PAPER • OPEN ACCESS

# Improved weighted sum estimation of total radiated power at W7-X

To cite this article: G. Partesotti *et al* 2025 *Nucl. Fusion* **65** 016035

OPEN ACCESS
IOP Publishing | International Atomic Energy Agency
Nuclear Fusion
Nucl. Fusion **65** (2025) 016035 (17pp)
https://doi.org/10.1088/1741-4326/ad9488

# Improved weighted sum estimation of total radiated power at W7-X

**G. Partesotti[1,*], F. Reimold[1], A. Tsikouras[1], D. Zhang[1], G. Kawamura[2,3], B.J. Peterson[2] and the W7-X Team[a]**

[1] Max-Planck-Institut für Plasmaphysik, Greifswald, Germany
[2] National Institute for Fusion Science, Toki, Japan
[3] National Institutes for Quantum Science and Technology, Rokkasho, Japan

E-mail: gabriele.partesotti@ipp.mpg.de

Received 31 July 2024, revised 5 November 2024
Accepted for publication 19 November 2024
Published 29 November 2024

**Abstract**

As magnetic confinement devices move toward higher fusion powers, moderating the heat load to the plasma-facing components becomes increasingly challenging. Efficient power dissipation can be achieved through control of the plasma radiation. However, defining a reliable proxy for the total radiated power is particularly challenging for non-axisymmetric devices such as stellarators. To address this problem, the radiated power can be estimated through a sum of the individual line-integrated bolometer measurements with weights properly calculated to account for the three-dimensional magnetic geometry. The present contribution aims to apply this weighted sum approach to Wendelstein 7-X (W7-X) and quantitatively validate it. First, we generate synthetic radiated power phantoms with characteristic W7-X radiation features to derive a set of optimized line-of-sight weights. Then, we test the weights on mock-ups and EMC3-EIRENE radiation patterns, including acquisition and analysis errors such as random noise fluctuations, camera misalignments, and field errors. Compared to other methods, the optimized weighted sum technique exhibited the best performance in all the presented synthetic test cases. When applied to experimental bolometer data, the optimized weights provided a proxy that is both reliable and real-time capable. Further validation is foreseen for the next experimental campaign.

Keywords: plasma, radiation, bolometer, power, stellarator

(Some figures may appear in colour only in the online journal)

## 1. Introduction

Plasma radiation can provide an efficient exhaust channel for the excess power entering the plasma scrape-off layer (SOL) [1]. In diverted devices in particular, plasma detachment can be exploited to reduce heat and particle fluxes at the target, mitigating erosion [2]. With sufficient SOL dissipation capabilities, limiting the radiative cooling to the edge is generally preferable to maintain high core temperatures. Accurate knowledge of the total plasma radiated power $P_{\mathrm{rad}}$ and its fraction $f_{\mathrm{rad}} = \frac{P_{\mathrm{rad}}}{P_{\mathrm{heat}}}$ to the input heating power $P_{\mathrm{heat}}$ is therefore crucial for accurate power balance studies, optimal performance, and the operation of future reactors.

Radiated power measurements are routinely performed by bolometers. In particular, resistive bolometer cameras measure the radiated power integrated within the detector line-of-sight (LoS) volume and over a wide spectral range [3]. Thanks to their reliability and fast (order of ms) time response,

[a] See Grulke *et al* 2024 (https://doi.org/10.1088/1741-4326/ad2f4d) for the W7-X Team.
[*] Author to whom any correspondence should be addressed.



 

bolometer measurements have already been employed as a feedback signal for divertor heat flux control systems based on impurity seeding actuators [4]. Several resistive bolometers are currently installed at W7-X: a divertor bolometry system (four cameras) [5], a core bolometry system (two cameras) [6], and three compact bolometer cameras (CBCs) [5].

When radiation tomography is available, the additional information on the radiated power density distribution can be used to define or refine the $P_{\mathrm{rad}}$ estimate. The radiation tomogram can also inform systems for the prevention and mitigation of disruption events in tokamaks [7]. However, tomographic inversions carry a considerable computational cost and are currently limited to mostly 2D distributions. For this reason, a simpler proxy is typically formulated as a function of one or many line-integrated bolometer measurements. Often the individual bolometer measurements are summed together with adequate weights [8], obtaining a fast (order of $\mu$s) and therefore real-time capable signal for $P_{\mathrm{rad}}$. In comparison, tomographic inversions of bolometry data at W7-X require a much longer run time (order of seconds or minutes) and are currently available only post-discharge.

In tokamak devices, full diagnostic coverage of one poloidal cross-section can be sufficient for a reliable $P_{\mathrm{rad}}$ estimation [9]. By taking advantage of the toroidal symmetry assumption, a geometrical average of the local bolometer power measurement can be extrapolated to the total $P_{\mathrm{rad}}$ through a multiplicative factor [10]. Such approximation is less applicable to stellarators, where significant variations of the radiated power density—or emissivity $\varepsilon$—are observed in the toroidal direction [11]. The toroidal asymmetry can be either intrinsic or derived from localized gas seeding sources [12–15].

At W7-X, studies on EMC3-EIRENE [16] simulations of impurity radiation show the possibility of a significant asymmetry of the radiated power density distribution over the 36° extent of the stellarator half-module. For typical plasma parameters, the simulated toroidal emissivity profile often peaks in the divertor region, especially at low $f_{\mathrm{rad}}$ [5]. These results are consistent with observations from the recently installed divertor bolometry system and the infra-red (imaging) video bolometer [17, 18] at W7-X. Both diagnostics provided experimental evidence of intense radiated power features toroidally confined to the divertor region, originating in the edge near the divertor target plates. The toroidal asymmetry poses an additional challenge to quantifying the total $P_{\mathrm{rad}}$, especially when the three-dimensional radiation distribution is not adequately diagnosed [5].

In the poloidal plane, the W7-X emissivity distribution can be both up-down and in-out asymmetric. More specifically, the up-down asymmetry generally dominates in plasmas at low density or low connection length and is commonly observed over many magnetic configurations and plasma conditions [19]. This asymmetry seems to be partly caused by $E \times B$ drift effects giving rise to an asymmetric distribution of plasma parameters (most importantly electron density and impurity density) [8, 20]. This picture is seemingly complicated by poloidally localized radiation regions whose location is not affected by field reversal, possibly associated with plasma-wall interaction sources [21]. Proper assessment of an asymmetrical poloidal radiation distribution requires full coverage of the plasma cross-section from multiple vantage points.

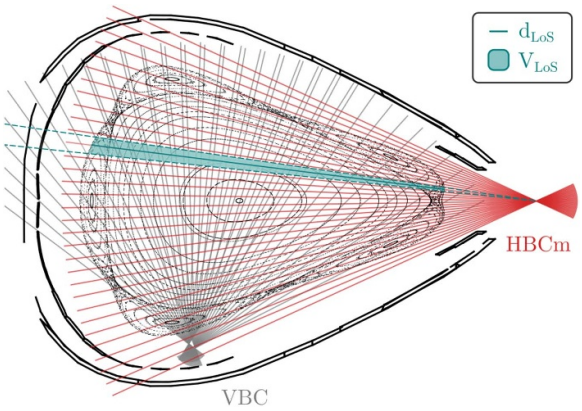


**Figure 1.** LoS geometry of the core bolometry system. The central LoS of the horizontal bolometer camera is highlighted in red, while the two vertical cameras are greyed out. The extent of one sightline in the poloidal plane is indicated with teal dashed lines. The teal-shaded area corresponds to the intersection of the sightline with the plasma volume. The LoS intersection length ($d_{\mathrm{LoS}}$) and volume ($V_{\mathrm{LoS}}$) are necessary for computing the local plasma emissivity averaged within the LoS (equation (2)).

The radiation distribution at W7-X is then fully three-dimensional, and asymmetrical both in poloidal and toroidal direction. It follows that an accurateJ evaluation of the total radiated power should ideally be based on multiple bolometer measurements from several toroidal locations and vantage points. Nonetheless, the current approach is based on the local average emissivity measured by a single bolometer in one poloidal cross-section. In particular, the $P_{\mathrm{rad}}$ proxy is provided by the horizontal bolometer camera (HBCm) which is located at the outboard midplane as part of the core bolometry system (red LoS in figure 1). The average local emissivity measurement from HBCm is then extended to the whole plasma volume. This is done by applying the simplification of axisymmetry, similarly to tokamaks [8]. A second camera—the vertical bolometer camera (VBC)—provides a lower vantage point (grey LoS in figure 1) for tomographic reconstructions and separation of the inboard-outboard radiation components.

In the Large Helical Device (LHD) on the other hand, the plasma radiated power was calculated as a weighted sum of the independent bolometer signals with optimized weights [13]. The weights for each LoS are optimized based on the bolometer response to a large set of synthetic data. Depending on the scope of the optimization, several cameras can be combined to yield a comprehensive estimate for the total $P_{\mathrm{rad}}$ or to quantify toroidal radiation asymmetries [12, 13]. The scope of this article is to develop and validate an optimized weighted sum approach for W7-X.

The study opens with a description of the various $P_{\mathrm{rad}}$ proxy techniques in section 2. Then, the generation of a synthetic

dataset and the weight optimization is detailed in section 3. Section 4 treats the validation of the weighted sum performance when applied to mock-up and EMC3-EIRENE radiation patterns, with added effects from random noise fluctuations and simulated camera misalignments or magnetic field errors. Finally, in section 5, the optimized weighted sum method is applied to experimental data to assess its performance in real W7-X plasma discharges.

## 2. Total radiated power proxy

Many different approaches can be used to link the bolometer measurements to a proxy for the total radiated power in a plasma device. In this article, we distinguish between three main methods: the average emissivity method [5] in section 2.1, the optimized weighted sum method [12] in section 2.2, and the tomographic method [8] in section 2.3. Lastly, section 2.4 discusses the advantages and disadvantages of the different methods in comparison to each other.

### 2.1. Average emissivity method

The procedure currently employed at W7-X for defining a $P_{\mathrm{rad}}$ proxy begins by computing the intersection between the bolometer sightlines and the plasma volume. For a given number of bolometer channels $n_{\mathrm{ch}}$, the intersection volumes $V_{\mathrm{LoS}}$ and lengths $d_{\mathrm{LoS}}$ along each detector LoS axis are obtained (see figure 1). Then, the chord brightness $\varepsilon_{\mathrm{chord}}$ ($\mathrm{Wm}^{-3}$) corresponding to each power measurement $p$ is calculated with

$$\varepsilon_{\mathrm{chord}} = \frac{4\pi}{d_{\mathrm{LoS}}\, e} p. \tag{1}$$

Here $e$ is the channel etendue ($\mathrm{m}^2\mathrm{sr}$), which is fixed by the camera construction [5]. The chord brightness is a measurement of the average plasma emissivity along the LoS, and is defined as the measured brightness normalized to the LoS length crossing the plasma volume. For a camera with $n_{\mathrm{ch}}$ sightlines, the independent chord brightness measurements can be averaged with $V_{\mathrm{LoS}}$ weights to obtain the average plasma emissivity within the camera field-of-view (FoV)

$$\langle \varepsilon \rangle = \frac{1}{\sum V_{\mathrm{LoS}}} \sum_{i=0}^{n_{\mathrm{ch}}} \varepsilon_{\mathrm{chord},i} V_{\mathrm{LoS},i}. \tag{2}$$

Now $\langle \varepsilon \rangle$ can be used to calculate a proxy for the total $P_{\mathrm{rad}}$ with a simple multiplication

$$P_{\langle \varepsilon \rangle} = \langle \varepsilon \rangle V_{\mathrm{plasma}} \tag{3}$$

when the plasma volume $V_{\mathrm{plasma}}$ is known [8]. Hence this method—hereby named the average emissivity method—relies on the assumption that $\langle \varepsilon \rangle$ is well representative of the real plasma emissivity, or that the emissivity presents a uniform distribution [5].

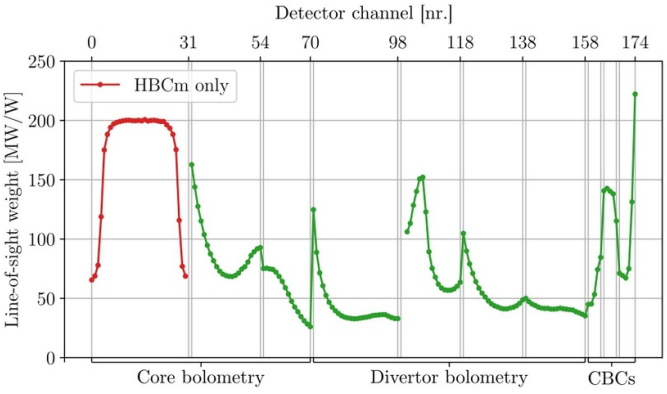


**Figure 2.** Bolometer line-of-sight weights for the average emissivity method (equation (5)). The weights corresponding to HBCm channels are highlighted in red. The LoS intersections are computed on the standard configuration plasma volume. The units are MW of total radiated power per W of the line-integrated measurement. Channels from different cameras are separated by vertical grey lines. Cameras are grouped depending on which bolometer system they belong to (core, divertor, or CBC).

Rearranging equations (1)–(3) this method can be seen as a weighted sum of the original line-integrated power measurements $p$

$$P_{\langle \varepsilon \rangle} = \sum_{i=0}^{n_{\mathrm{ch}}} w_{\langle \varepsilon \rangle, i} p_i \tag{4}$$

with weights

$$w_{\langle \varepsilon \rangle} = \frac{4\pi}{d_{\mathrm{LoS}}\, e} \frac{V_{\mathrm{LoS}}}{\sum V_{\mathrm{LoS}}} V_{\mathrm{plasma}}. \tag{5}$$

Figure 2 reports the $w_{\langle \varepsilon \rangle}$ for all the resistive bolometer channels currently installed in W7-X with standard magnetic field configuration.

The available sightlines are:

- 71 core bolometry channels: 2 cameras, [32, 24+15]
- 88 divertor bolometry channels: 4 cameras, [28, 20, 20, 20]
- 16 CBC channels: 3 cameras, [5, 5, 6] (corresponding to CBCs #2, #3, and #4 in [5])

for a total of 175 resistive bolometer channels.

### 2.2. Optimized weighted sum method

An established approach to take into account the three-dimensional magnetic field geometry of stellarators for the $P_{\mathrm{rad}}$ proxy is the optimized weighted sum (ws) method. In this case, the total radiated power is expressed as a generalized weighted summation of a given number $n_{\mathrm{ch}}$ of bolometer measurements

$$P_{\mathrm{ws}} = \sum_{i=0}^{n_{\mathrm{ch}}} w_{\mathrm{ws},i} p_i. \tag{6}$$

The difference to equation (4) is that the individual LoS weights $w_{\mathrm{ws}}$ are not calculated by relevant physical dimensions

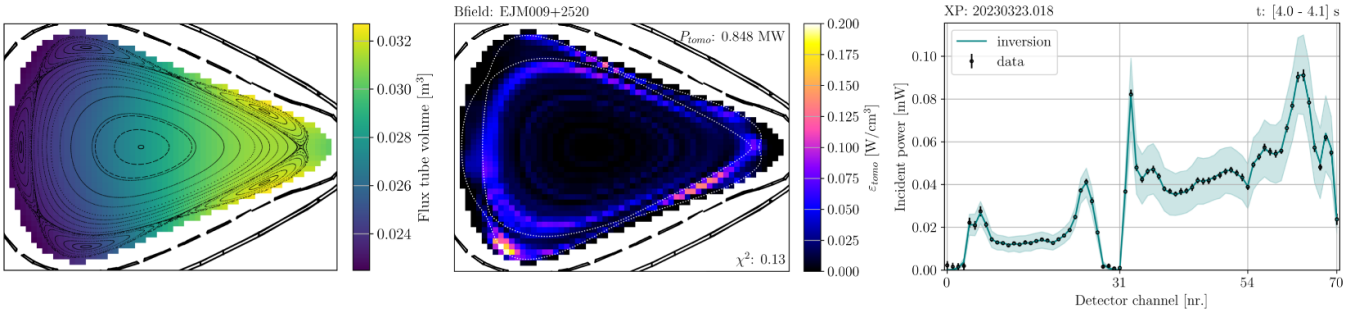


(a) Mesh volumes (b) Tomographic inversion (c) Bolometer measurement

**Figure 3.** (*a*) Poloidal distribution of the flux tube volumes on a field-aligned 3D mesh. The volumes are calculated over a stellarator module in standard magnetic field configuration. Due to stellarator symmetry, they are up-down symmetric in the $(R, z)$ plane. A cross-sectional cut of the W7-X vessel wall is indicated with black lines. A Poincaré visualization of the standard magnetic field geometry is superimposed on the contour plot. (*b*) Radiation distribution in the triangular plane reconstructed from a plasma discharge using relative gradient smoothing-Gaussian process tomography. The magnetic field geometry is set to standard configuration (magnetic islands overlaid as a dotted white line). (*c*) Corresponding line-integrated measurement used for the tomographic reconstruction (black markers) and line-integrals on the reconstructed pattern (teal line). The standard deviation on the reconstructed line integrals is plotted as a shaded area.

of shape and size, but are optimized based on a training dataset. The $w_{\mathrm{ws}}$ weights are determined by the modeled detector response to synthetic data of which the underlying $P_{\mathrm{rad}}$ value is known.

Given a large set of $N$ synthetic radiated power measurements, we can name $b$ the vector of the corresponding total radiated power values. We can forward calculate the line-integrals $p$ and group them in a matrix $A$ of shape $n_{\mathrm{ch}} \times N$. For a temporary weight set $x$, the product $A \cdot x$ identifies the vector of calculated proxies. The optimal weights can be identified through a minimization of the residuals to the target vector $b$

$$w_{\mathrm{ws}} = \min ||A \cdot x - b||^2 + \lambda ||x||^2 \tag{7}$$

also known as Tikhonov regularization [22]. The factor $\lambda$ is a regularization parameter that can be used to control the smoothness of the solution. The smoothing effect enhances the robustness of the method at the cost of information loss and, therefore, lower precision.

A direct numerical solution to equation (7) can be found via

$$x = \left(A^{\mathrm{T}} A + \lambda \mathrm{I}\right)^{-1} A^{\mathrm{T}} b \tag{8}$$

where I is the identity matrix [12].

### 2.3. Tomographic method

An alternative total radiated power proxy technique is the so-called tomographic estimate $P_{\mathrm{tomo}}$. This requires performing tomography inversion of the bolometer line-integrated data in one poloidal cross-section to retrieve the two-dimensional radiated power density distribution $\varepsilon_{\mathrm{tomo}}$. Under the assumption of toroidal symmetry, the total radiated power can be inferred by extending the 2D distribution toroidally to the whole plasma volume. In practice, the emissivity value $\varepsilon_{\mathrm{tomo},i}$ of each pixel in the reconstructed tomogram is multiplied by volume $V_i$ of the corresponding flux tube in 3D space. Then, all these radiated power contributions are summed together. For an inversion grid composed of $n$ voxels:

$$P_{\mathrm{tomo}} = \sum_{i=0}^{n} \varepsilon_{\mathrm{tomo},i} V_i. \tag{9}$$

Said procedure is particularly effective in tokamak machines, where the approximation of axisymmetry is often valid [23]. Since the voxel mesh covers the whole radiating plasma volume: $\sum_{i=0}^{n} V_i = V_{\mathrm{plasma}}$.

As shown in figure 3(*a*), the poloidal distribution of the flux tube volumes exhibits an inverse dependence with the major radius coordinate. In other words, plasma voxels on the outboard side yield a relatively larger contribution to the full torus radiated power $P_{\mathrm{rad}}$. By using the spatial distribution of the emissivity $\varepsilon_{\mathrm{tomo}}$ instead of its average value within the camera FoV $\langle\varepsilon\rangle$, these volume effects are taken into account. Thus, $P_{\mathrm{tomo}}$ (equation (9)) can be seen as a refinement of $P_{\langle\varepsilon\rangle}$ (equation (3)). The additional knowledge on the distribution provided by tomography with multiple vantage points allows a more precise $P_{\mathrm{rad}}$ estimation.

It is relevant to point out that the reconstructed emissivity map $\varepsilon_{\mathrm{tomo}}$ generally deviates from the true distribution $\varepsilon$. Several factors come into play to define this tomographic error, such as the intrinsic uncertainty of the applied inversion algorithm, quality of the diagnostic coverage, and experimental noise level. Radiation tomography at W7-X is currently performed on the core bolometry system, which is located in one triangular symmetry plane [6]. In this paper, tomographic inversions are performed using a Gaussian process tomography (GPT) [18] algorithm. To improve tomographic reconstructions, a relative gradient smoothing (RGS) [8] factor is introduced in the prior model, together with smoothing of the emissivity distribution in radial and poloidal direction. One example tomogram reconstructed using the RGS-GPT solution is shown in figure 3(*b*). This is a typical radiation distribution observed in the triangular plane in standard magnetic field configuration during attached, steady-state

conditions with no impurity seeding. Next to it in in figure 3(*c*) is reported its associated bolometer measurement.

### 2.4. Discussion on the various methods

From equations (2) and (3) we see that the average emissivity estimate for $P_{\mathrm{rad}}$ depends on some fixed and measurable, physical quantities. Furthermore, $P_{\langle\varepsilon\rangle}$ is positive definite and always proportional to the line-integrated data. This characterizes the average emissivity approach as a simple and robust method. The caveat is that the geometrical parameters $d_{\mathrm{LoS}}$, $V_{\mathrm{LoS}}$, and $V_{\mathrm{plasma}}$ need to be determined case-by-case for every magnetic configuration. These parameters can also be subjected to deviations from the assumed plasma or camera geometry (e.g. error fields, camera misalignments, iota corrections due to a change in plasma current).

When applying equation (2) to compute the average emissivity, any number of sightlines can be employed. However, full sampling of at least one plasma poloidal cross-section is required. At W7-X, the collection of HBCm channels ($n_{\mathrm{ch}} = 32$, figure 1) is found to yield the best results of any individual camera. Hence—as mentioned at the end of in section 1—this is the commonly used $P_{\mathrm{rad}}$ proxy for W7-X. In this paper we label the average emissivity proxy calculated on the 32 HBCm channels as $P_{\langle\varepsilon\rangle\mathrm{HBCm}}$.

The symmetrical set-up of fan-shaped LoS geometry on the triangular cross-section provides a uniform distribution of $d_{\mathrm{LoS}}$, $V_{\mathrm{LoS}}$ parameters, as shown on the left-hand side of figure 2 (red line). As a consequence, all sightlines (except for the very upper or lower ones near the SOL edge) are weighted approximately the same. This mitigates inaccuracies arising from noisy or miscalibrated LoS and very localized signals. Nonetheless, the HBCm proxy $P_{\langle\varepsilon\rangle\mathrm{HBCm}}$ is prone to large errors when the poloidal radiation pattern is in-out asymmetric, due to the uneven LoS density distribution across the triangular cross-section. Radiation sources at the inboard side tend to be underestimated, while emission at the outboard vertex tends to be overestimated. appendix reports an analysis of the uncertainty on $P_{\langle\varepsilon\rangle\mathrm{HBCm}}$ when applied to synthetic data. Of course the same reasoning applies to up-down asymmetric patterns (lower side overestimated, upper side underestimated) when VBC is utilized [24]. One solution to this issue is provided by the tomographic method. Radiation tomography takes into account the vantage point of each camera to provide a more objective assessment of the emissivity distribution.

As explained in section 2.1, equation (3) implies a uniform plasma emissivity throughout the plasma volume $V_{\mathrm{plasma}}$. Hence, in toroidally asymmetric conditions, extrapolating the average emissivity quantified from a single toroidally localized diagnostic will inevitably lead to inaccuracies [5]. This is the case for HBCm, whose toroidal coverage of the half-module is only $\Delta\varphi < 5°$. One way to mitigate this error could be diagnosing a larger portion of the plasma volume with more bolometer sightlines. In W7-X, multiple bolometer cameras in different toroidal locations are available (core system, divertor system, and CBCs). Their chord brightness measurements can be combined with HBCm into the summation of equation (4) using their respective weights $w_{\langle\varepsilon\rangle}$ (green line in figure 2). When all the 175 available channels mentioned at the end of section 2.1 are used in the average emissivity method the resulting proxy is named $P_{\langle\varepsilon\rangle\mathrm{TOT}}$.

Even still, a proper assessment of the average emissivity using $P_{\langle\varepsilon\rangle\mathrm{TOT}}$ would require an ideally uniform coverage of the plasma volume—or at least of one stellarator half-module. In the current W7-X bolometry layout, some regions of the half-module are sampled with a high LoS density, while other regions are not observed at all (visualized later in figure 7). Multiple sightlines intersecting the same region of space will skew the $\langle\varepsilon\rangle$ estimate towards their local chord brightness measurement. Conversely, the emissivity of regions that are not sampled or poorly sampled will not be represented in the total $\langle\varepsilon\rangle$. This is the issue of oversampling vs. undersampling of the emission volume. For this reason, adding more sightlines into the summation does not necessarily improve the average emissivity estimate on a three-dimensional radiating structure. When adding a new bolometer channel, the amount of new information carried by the new LoS has to be taken into account. This is the line of action taken by the optimized weighted sum method.

It can be noticed how the optimal weights $w_{\mathrm{ws}}$ are the ones that minimize the *total* residual in equation (7). As a consequence, they will depend not only on the radiation features selected for the training (*a priori* information), but also on the particular set of $n_{\mathrm{ch}}$ selected sightlines. Each time the set of LoS is updated, a new run of the optimization routine is required to calculate the new coefficients. The upside is that the weights $w_{\mathrm{ws}}$ are adjusted each time taking into account overlaps in the LoS coverage. Once calculated, the $w_{\mathrm{ws}}$ weights are optimized to interpolate and extrapolate between oversampled and undersampled regions based on the training radiation profiles. Assuming the synthetic radiated power distributions used in the optimization can be trusted, the weighted sum approach is thus able to compensate for the lack of coverage and double counting. Still, correctly assessing asymmetric distributions with strong (toroidal and poloidal) emissivity gradients remains especially challenging.

The optimization ensures that small weights are assigned to channels characterized by a low signal-to-noise ratio or ones that carry little information. These channels then have a small impact on the total $P_{\mathrm{rad}}$. Following this logic, the weighted sum method can also be used to identify 'relevant' sightlines that carry most of the information. For instance, bolometer data could be streamed to the W7-X control system to design a real-time feedback loop. A hardware implementation of this would allow only a limited number of channels, which can be selected accordingly. However, using a reduced set of channels typically decreases the accuracy of the $P_{\mathrm{ws}}$ proxy. In LHD, a single wide-angle resistive bolometer channel—and associated weighting factor—was found to provide a sufficiently good approximation for the total radiated power [13].

Lastly, when two or more bolometer cameras are toroidally separated (as in our case), an optimized coefficient set can be computed for each camera separately to retrieve multiple $P_{\mathrm{ws}}$ estimates. If the weights are optimized for toroidally symmetric radiation patterns but the experimental $P_{\mathrm{ws}}$ values show a trend as a function of $\varphi$, their profile can be used to assess

the underlying toroidal asymmetry [12]. Alternatively, the toroidal profile of the radiated power density can be traced by using the average emissivity method [5]. Essentially the average poloidal emissivity estimated from several toroidally localized measurements is compared. However, this requires full coverage of the emission volume in the poloidal plane.

It must be pointed out that the increased flexibility in the choice of weights $w_{ws}$ comes at a price. The weighted sum method can yield a largely incorrect—or even unphysical (negative)—$P_{ws}$ output if applied to cases that significantly differ from the cases contained in the training dataset. This kind of unreliable behavior is similar to using a machine learning model to predict values that lie outside its training range. For this reason, the dataset choice is crucial. The more features that are introduced in the synthetic dataset, the more robust the method will be when applied to various plasma scenarios. However, there is a trade-off. A more generalized response also leads to loss of precision. Furthermore, including non-physically justified elements is particularly detrimental since it optimizes the solution for unrealistic cases. Hence, an ideal training dataset should contain all and only the fundamental radiation attributes and behaviors that are expected in the experiment. In the following section—section 3—we delve into the topic of how to define an accurate training scheme.

## 3. Optimization of LoS weights

The objective of the weighted sum method is to produce a reliable proxy $P_{ws}$ for the total radiated power $P_{rad}$ that is optimized based on the expected plasma characteristics. Following equation (7), this requires defining a set of synthetic line-integrated measurements $A$ and the respective $P_{rad}$ values $b$. In the following section, we detail the process of weights optimization. Section 3.1 deals with definition of a training dataset, while the weights themselves are calculated in section 3.2.

### 3.1. Dataset generation

Several different sources of radiation data can be used to construct a training dataset. At LHD, the summation weights $w_{ws}$ were optimized based on EMC3-EIRENE simulations of deuterium or impurity radiation at various plasma parameters, plus a core radiation contribution [12]. Alternatively, 2D or 3D tomographic inversions of experimental bolometer data could be used if available. For this study, a large set of mock-up emissivity phantoms is utilized to have full control over the optimization input. Each mock-up is generated on a three-dimensional field-aligned grid. The grid is obtained by tracing the coordinates of each voxel corner along the magnetic field lines [5]. Only the standard magnetic field configuration is treated here ($V_{plasma} = 43.5\,m^3$).

The total $P_{rad}$ contribution of each mesh element is determined by the product of its volume and emissivity value. Figure 4 shows the total sum of mesh volumes in each poloidal slice plotted as a function of the toroidal coordinate. They are on average larger in the divertor region, namely within $\varphi = 0°$–$18°$ and $\varphi = 54°$–$72°$, with a relative difference of

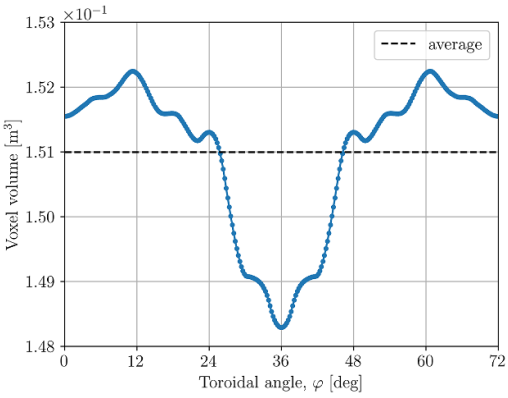


**Figure 4.** Toroidal distribution of the voxel volumes across one stellarator half-module. The overall variation amounts to $\pm 1\%$.

$\pm 1\%$. Thus, there is no inherent toroidal asymmetry of radiated power density due to the volume distribution. In the poloidal plane (figure 3(*a*)) the difference is larger—up to roughly $\pm 20\%$. Here a direct major radius dependence emerges, with the flux tubes corresponding to pixels on the outboard side presenting the largest volumes.

We identify a set of 48 basic radiation features from a combination of EMC3-EIRENE-simulated and experimental radiated power data [5, 8, 21]. The mock-up patterns replicating these features—named archetypes—can be subdivided into 34 edge emission cases and 14 core emission cases. The edge archetypes contain *X*-/*O*-point radiation, EMC3-EIRENE-like island emission, and broader flux surface-aligned rings of different uniformity. The core archetypes contain various core peaking cases and flux surface-confined emission rings. Both symmetric and (in-out or up-down) poloidal asymmetric patterns are also present. Some of these features are typical of steady-state plasmas, and some are more transient (e.g. following laser blow-off (LBO) or pellet injections of impurities). Figure 19 in the appendix illustrates all of them. All archetypes are defined as a function of the Variational Moments Equilibrium Code [25] coordinates on the three-dimensional mesh and therefore follow the equilibrium flux surface geometry. The total radiated power associated with each of them is $P_{rad} = 1\,MW$ (except for 'Null' archetypes).

Each emissivity phantom composing our training dataset is a generated as a random linear combination of two edge archetypes and two core archetypes. At every iteration, the archetype distributions are randomly picked and summed together with scaling factors for the emissivity. The four scaling factors of the linear combination are also random numbers $[a,b,c,d] \in [0,1] \subset \mathbb{R}$. Consequently, the relative contribution of each archetype to the phantom is randomized, and the total underlying total radiated power is a random value comprised between $P_{rad} = 0$–$4\,MW$. This procedure is repeated for $N = 1\,000\,000$ phantoms to ensure good statistics in the dataset.

Figure 5(*a*) reports the average emissivity pattern, obtained by averaging the 1 000 000 phantoms together. This distribution does not change upon changing the random seed. Moreover, the distribution of radiated power values—reported

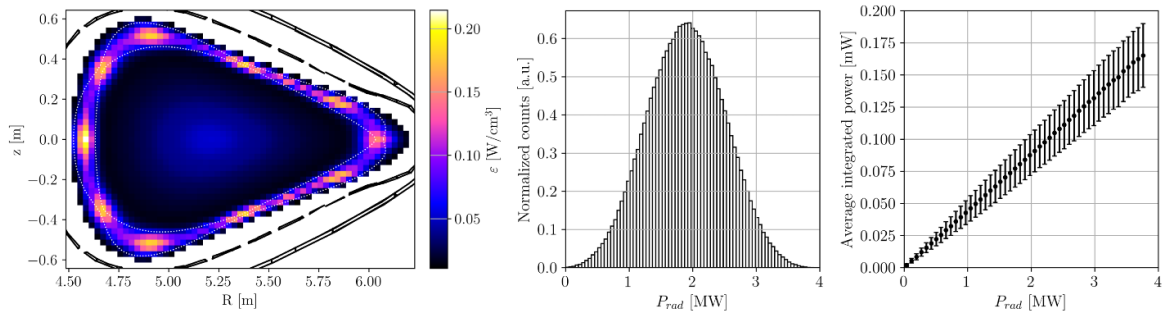


(a) Merged phantom (b) Dataset $P_{rad}$ distribution (c) Average bolometer signal

**Figure 5.** (*a*) Average dataset phantom obtained by merging the 1000 000 mock-up phantoms composing the training dataset. Each entry generated as a random combination of two edge and two core radiation archetypes. The standard magnetic island geometry is visualized using dotted white lines. (*b*) Histogram of the reference $P_{\mathrm{rad}}$ values. The $P_{\mathrm{rad}}$ distribution is Gaussian, covering the 0–4 MW range. Due to the presence of zero radiation patterns ('Null'), the average is shifted below 2 MW. (*c*) Line-integrated bolometer measurement as a function of $P_{\mathrm{rad}}$, averaged over all resistive (non-CBC) channels and all mock-up phantoms.

in figure 5(*b*)—is appropriately Gaussian. This means that 1000 000 phantoms are sufficiently statistic. As expected, the distribution resulting from merging all phantoms is up-down symmetric and presents both edge and core radiation with a combination of different island emission elements. Since the individual phantoms contain only four archetypes, they are much less structured than this. The radiated power density of the merged distribution tends to peak in the edge region, but the overall fraction of radiated power is roughly equally distributed between SOL and core volume. These characteristics are realistic for most of the plasma scenarios [8]. It can be noticed that the merged phantom presents an inboard-dominant asymmetric distribution of the emissivity. This is a purely geometrical effect that arises from the *X*-/*O*-point disposition in the triangular plane. Every pair of asymmetric archetypes (e.g. 'Op4' and 'Xp1' in figure 19) is generated using the same function of magnetic coordinates and the same amount of radiated power.

The relationship between the radiated power density distribution $\varepsilon$ on the voxel mesh to a set of line-integrated power values $p$ (W) on each detector is defined by the geometry—or transfer—matrix $G$ (m$^3$) of the system [5]

$$p = \sum_{j=0}^{n} G_j \varepsilon_j + \sigma \tag{10}$$

where $\sigma$ is random fluctuations artificially included in the forward calculated synthetic measurement. This simulates experimental noise, making the method more robust and generally applicable. Added noise produces a similar outcome in the weights to the regularization parameter $\lambda$. For this study, two separate error components are simulated. The first component is random fluctuations proportional to the line integral, mostly due to calibration errors. The second component is a background (flat) noise level, caused by electronic interferences (depends on acquisition hardware, quality of the housing and cable shielding, integration time). For the W7-X resistive bolometer systems, the proportional component is equal to 2% the $p$ value, and the magnitude of the background noise (measured pre-discharge) is 1 $\mu$W [8]. A conservative value of

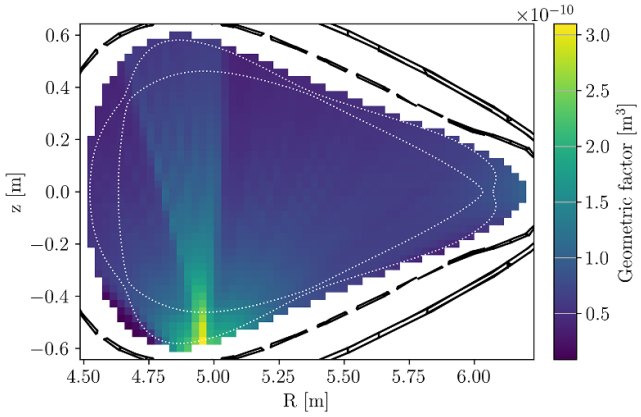


**Figure 6.** Geometry matrix of the core bolometry system interpolated on a field-aligned grid traced on the standard W7-X configuration.

respectively 5% and 2 $\mu$W is used in this study to take into account the possibility of outliers or degradation of the system with time.

In this case, the collection $A$ of measurements makes up a matrix of size (175 $\times$ 1000 000), while the target total radiated power values $b$ form an array of size 1000 000. A typical resistive bolometer measurement in this $P_{\mathrm{rad}}$ = 0–4 MW range is of the order of $10^{-4}$ W, as shown in figure 5(*c*). $A$ and $b$ together form what is called the training dataset.

As an example, figure 6 illustrates the geometry matrix of the core bolometry system (see sightline plot of figure 1) interpolated on a standard configuration field-aligned grid.

Intuitively, the geometric factor identifies the contribution of each voxel emissivity to each bolometer channel. By summing up the geometry matrix of one diagnostic in the poloidal plane and plotting this value toroidally, we can visualize how its LoS density changes across the stellarator half-module. This picture is reported in figure 7. It can be noticed how some toroidal intervals (e.g. quasi-bean plane at $\varphi = 14°$ and triangular plane at $\varphi = 36°$ are sampled with a high LoS density. On the contrary other areas (e.g. $\varphi = 0°$–$12°$ or $\varphi = 22°$–$32°$) are not sampled at all.

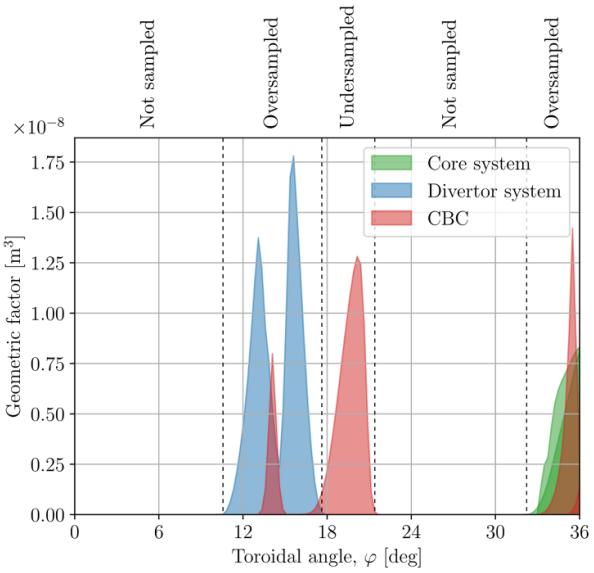


**Figure 7.** Geometric factor inside the plasma volume for the W7-X resistive bolometers as a function of the toroidal angle within a stellarator half-module, assuming stellarator symmetry. Different colors identify different diagnostics: divertor system (blue) core system (green), and CBCs (red). Good LoS coverage is provided in the quasi-bean plane ($\varphi = 14°$) and the triangular plane ($\varphi = 36°$). Other plasma regions that are either more sparsely covered ($\varphi = 14°$), or not covered at all ($\varphi = 0°$–$10°$ and $\varphi = 22°$–$32°$).

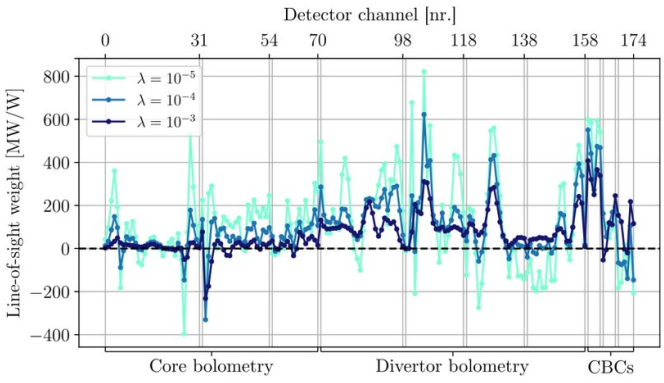


**Figure 8.** Bolometer line-of-sight weights for the weighted sum method. Different shades of blue correspond to different regularization levels. Higher regularization coefficients $\lambda$ (equation (8)) reduce the channel-to-channel variations.

The toroidal distribution of the emissivity phantom is controlled by individually rescaling each poloidal slice of the three-dimensional geometry matrix $G$. Each poloidal slice of $G$ is multiplied by the modifier value (a positive definite number) and is therefore rescaled without affecting the poloidal distribution. This has the same effect on $p$ as if the toroidal asymmetry was intrinsic to the emissivity pattern $\varepsilon$, since $G$ is effectively a prefactor (see equation (10)). The collection of toroidal rescaling factors is randomly picked from a pool of nine different toroidal profile modifier curves, illustrated in figure 20 in the appendix. The case of no toroidal asymmetry corresponds to a flat modifier curve of unit values (figure 20(*i*)).

Every toroidal profile modifier curve is defined based on the toroidal emissivity distribution resulting from an EMC3-EIRENE simulation of intrinsic carbon impurity radiation. Different curves are associated to different settings in the simulation such as electron density at the separatrix $n_{\mathrm{sep}}$, heating power $P_{\mathrm{heat}}$, and radiated power $P_{\mathrm{rad}}$. First, the EMC3-EIRENE emissivity distribution is averaged poloidally and fitted using a polynomial function. Then the fitted values are normalized to their total sum so that the total radiated power is conserved during the rescaling. Hence, these modifiers have the effect of reshaping the toroidal distribution of the geometry matrix to reflect one of several EMC3-EIRENE toroidal asymmetries of the plasma emissivity. Experimentally, a variety of radiating species is present, as well as effects that are not captured by the simulation code (e.g. particle drifts).

The nine toroidal profile modifiers show various peaking locations (divertor region, core region, or in between) and asymmetry degrees, from $\pm 30\%$ (maximum asymmetry) to $\pm 0\%$ (no asymmetry). Since most of the EMC3-EIRENE intrinsic carbon emission runs show a divertor-dominant toroidal distribution, the majority of the profiles peak in the divertor region. Peaking in the core region is more seldomly encountered for typical W7-X operational parameters and is therefore less represented.

### 3.2. Calculation of weights

We now compute a set of LoS weights $w_{\mathrm{ws}}$ using equation (8). Figure 8 shows the comparison of the weights set at different regularization levels ($\lambda = [10^{-5}, 10^{-4}, 10^{-3}]$). As shown in figure 8, the LoS coefficients are mostly positive, with a few negative values and larger variance compared with $w_{\langle\varepsilon\rangle}$ (see figure 2). For a given channel, a large $w_{\mathrm{ws}}$ factor does not necessarily mean a significant contribution of this channel measurement to $P_{\mathrm{ws}}$. This is due to the different detector geometries. The dependence of the weights on the particular seed used for generating the training dataset—namely the line integrals $A$ and the corresponding $P_{\mathrm{rad}}$ values $b$—is negligible. In other words, fluctuations of $w_{\mathrm{ws}}$ between neighboring channels are not a consequence of random noise but an inherent result of the optimization.

One explanation for the negative $w_{\mathrm{ws}}$ values is that they offer compensation for double counting due to LoS overlaps. This becomes clearer when focusing on the HBCm portion of the weights (red line in figure 2). The average emissivity weights $w_{\langle\varepsilon\rangle}$ reflect the symmetric geometry of HBCm, while $w_{\mathrm{ws}}$ are left-to-right asymmetric. Since the phantoms do not introduce an intrinsic up-down asymmetry in the training process, the asymmetry must derive from the correlation of the HBCm signal with other camera signals. The HBCm weights $w_{\mathrm{ws}}$ would be symmetric only if they were optimized in an isolated case.

At higher applied regularization (see figure 8 darker blue lines), the channel-to-channel gradients are reduced as well as the scale. Increasing the regularization factor further has the effect of flattening the weights over the majority of the sight-lines. This is a generally undesirable solution since it relies on

a small selection of 'relevant' channels (in this case the CBCs). As shown in section 4, a low-regularization set of weights exhibits an evident drop in performance when applied to measurements that deviate only slightly from the training conditions. In the following validation analysis, we select a value of $\lambda = 10^{-4}$. This is later compared to other methods in order to assess the individual robustness, accuracy, and precision of each proxy.

## 4. Validation

Here the performance of the various proxies are evaluated and compared to each other. The comparison is based on synthetic datasets, isolating different sources of error. Section 4.1 begins with the case of toroidally symmetric and asymmetric phantoms. Then, errors in the assumed camera-plasma geometry (either from the LoS or the field configuration) are introduced in section 4.2. Lastly in section 4.3, the proxies are tested on 3D distributions of impurity radiation computed from EMC3-EIRENE.

### 4.1. Mock-up phantoms

A test of the method performance can be carried out by applying the computed weights to synthetic data for which $P_{\text{rad}}$ is known exactly. The accuracy to which the total radiated power information can be recovered is the metric for defining the reliability and robustness of the proxy. At the same time, the validation results can be used to tune the parameters that define the optimization procedure (in this case $\lambda$). For the weighted sum technique, the test dataset should differ from the dataset used to optimize the weights (line-integrals $A$ and total radiated power values $b$ in equation (7)). To this end, a new dataset of 100 000 phantoms is now generated following the same logic described in section 3.1. Since the new dataset originates from a new random seed, its phantoms will carry all the same basic distribution features expressed in different random combinations.

We begin by comparing the optimized weighted sum proxy for the total radiated power $P_{\text{ws}}$ to two alternatives: the average emissivity proxy using only the 32 HBCm channels (current approach) and the one making use of all the 175 available channels. As mentioned in section 2.3, these are labeled $P_{\langle\varepsilon\rangle\text{HBCm}}$ and $P_{\langle\varepsilon\rangle\text{TOT}}$ respectively. We disregard the tomographic proxy due to its results being strongly dependent on the inversion method and the suitability of the prior model assumptions. Furthermore, computed tomography is often computationally expensive and therefore not real-time capable. For these reasons, the performance $P_{\text{tomo}}$ is not addressed in this validation study. Figure 9 presents a summary of the results from this first test.

An exact proxy would lie on the $y = x$ dashed line, which symbolizes agreement with the reference. A difference in slope to this line represents a systematic offset to the true $P_{\text{rad}}$, while the spread of the scatter is the inaccuracy of the proxy. It is evident from this overview how the optimized weighted sum technique $P_{\text{ws}}$ provides the most exact proxy by far out of

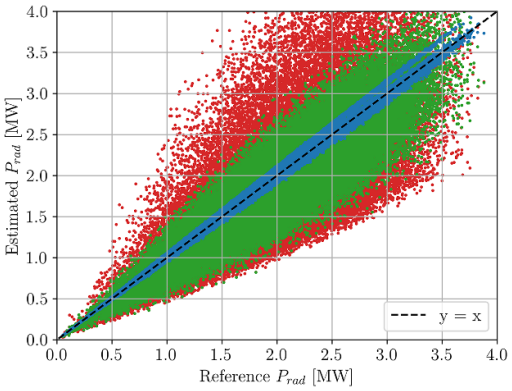


**Figure 9.** Total radiated power estimate from various proxy methods on toroidally asymmetric mock-up phantoms: HBCm-only average emissivity (red), all-channels average emissivity (green), and all-channels weighted sum (blue). The proxy is plotted against the corresponding $P_{\text{rad}}$ reference. A dashed line indicates the exact $y = x$ solution.

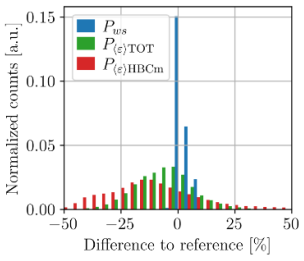


(a) Histogram of error $\delta$

| Tor. asym. mock-ups | |
|---|---|
| $\delta_{\langle\varepsilon\rangle\text{HBCm}}$ | $-7.3 \pm 24.0\,\%$ |
| $\delta_{\langle\varepsilon\rangle\text{TOT}}$ | $-6.1 \pm 12.6\,\%$ |
| $\delta_{ws}$ | $-0.05 \pm 2.16\,\%$ |

(b) Averaged error $\delta$

**Figure 10.** Relative percentage error results for the validation case: toroidally asymmetric mock-ups.

the three approaches. The second best is $P_{\langle\varepsilon\rangle\text{TOT}}$ (color-coded green), the all-channel average emissivity proxy. It follows the HBCm-only average emissivity proxy $P_{\langle\varepsilon\rangle\text{HBCm}}$ (color-coded red), which is provides the least reliable estimate in this case.

As expected, the proxy inaccuracy is proportional to the total radiated power in question. To get a quantitative estimate of the fidelity of each method, the discrepancy between each proxy and the associated $P_{\text{rad}}$ reference is expressed as a relative percentage error, denoted with $\delta$. Generating a different test dataset of phantoms (with a different random seed) has a negligible effect on the $\delta$ values. The $\delta$ variation is usually $< 0.1\%$, which is assumed to be the error bar for these evaluations. A histogram of all the 100 000 $\delta$ values is illustrated in figure 10($a$).

To summarize the outcome of the test, we average the relative percentage error $\delta$ over all samples and express it in terms of its mean value and standard deviation. These values are noted in figure 10($b$) below, and visualized as the first entry in in the overview plot reported later in figure 17. Here the higher performance of the optimized weighted sum method (third row) is signified by the lower average value and standard deviation of $\delta$ compared to the alternative methods.

Regarding the other proxy methods, $P_{\langle\varepsilon\rangle\text{HBcm}}$ can be quite reliable in approximately toroidally symmetric conditions when the local HBCm measurement is representative

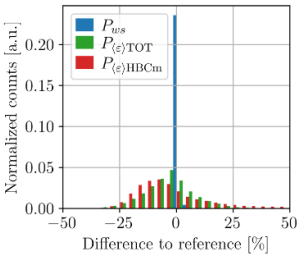


(a) Histogram of error $\delta$

| Tor. sym. mock-ups | |
|---|---|
| $\delta_{\langle\varepsilon\rangle\mathrm{HBCm}}$ | $+1.2 \pm 21.4\,\%$ |
| $\delta_{\langle\varepsilon\rangle\mathrm{TOT}}$ | $-2.8 \pm 11.0\,\%$ |
| $\delta_{ws}$ | $-1.2 \pm 0.5\,\%$ |

(b) Averaged error $\delta$

**Figure 11.** Relative percentage error results for the validation case: toroidally symmetric mock-ups.

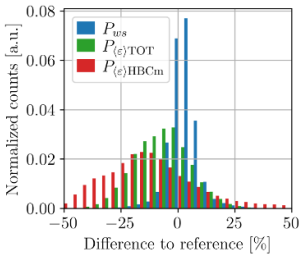


(a) Histogram of error $\delta$

| Tor. asym. mock-ups + LoS mis. | |
|---|---|
| $\delta_{\langle\varepsilon\rangle\mathrm{HBCm}}$ | $-8.5 \pm 23.9\,\%$ |
| $\delta_{\langle\varepsilon\rangle\mathrm{TOT}}$ | $-6.8 \pm 12.1\,\%$ |
| $\delta_{ws}$ | $+0.6 \pm 6.2\,\%$ |

(b) Averaged error $\delta$

**Figure 12.** Relative percentage error results for the validation case: toroidally asymmetric mock-ups with LoS misalignments.

of the average plasma emissivity (e.g. in the core or at radiation detachment). In these cases most of the toroidal profiles are divertor-dominant (figure 20 in the appendix), and $P_{\langle\varepsilon\rangle\mathrm{HBcm}}$ tends to underestimate the real $\langle\varepsilon\rangle$. With $P_{\langle\varepsilon\rangle\mathrm{TOT}}$, more sightlines and vantage points are available. As a result, the proxy performance is improved significantly. However, the current diagnostic setup in W7-X completely lacks bolometer sightlines over large sections of the half-module (see figure 7, and the $\delta_{\langle\varepsilon\rangle\mathrm{TOT}}$ error is still greatly affected by a non-uniform toroidal distribution. A $> 5\%$ deviation would still be unacceptable in a reactor-relevant scenario such as in the Demonstration Power Plant (DEMO) [1, 26, 27].

We conclude with a second test performed on a dataset of toroidally uniform mock-up phantoms. Only a flat toroidal profile modifier is applied here in the dataset generation routine (figure 20(*i*) in the appendix). The objective is to test the optimized weighted sum performance—which is trained in the presence of toroidal asymmetries—on a simpler toroidally symmetric case instead. As before, the results in terms of relative percentage error $\delta$ are reported visually in the overview in figure 11(*a*) (second entry of figure 17) and numerically in figure 11(*b*). We observe no significant degradation of the optimized weighted sum proxy compared to the previous case, which indicates good robustness.

### 4.2. *Effect of geometry errors*

As described in section 3.2, random noise fluctuations of the line-integrated signal are artificially included in the analysis. Experimentally, a second source of errors is related to uncertainty in the geometry of the bolometer LoS with respect to the plasma. These can be due to either a misalignment of the camera sightlines or a deviation from the assumed magnetic field configuration. Such errors would affect the LoS geometrical parameters ($d_{\mathrm{LoS}}$, $V_{\mathrm{LoS}}$, and $V_{\mathrm{plasma}}$) that determine $w_{\langle\varepsilon\rangle}$ in equation (5). The optimized weighted sum would also be affected since the assumed geometry ultimately determines the weights $w_{\mathrm{ws}}$ in equation (7).

First, we discuss sightline misalignments. These can be due to miscalibration of the foil position and FoV, which is measured in the vented vessel and based on CAD data. Manufacturing tolerances and a rigid movement or bend of the diagnostic immersion tube after pump-down can also give rise to misalignments. The expected magnitude of this effect is of the order of a few degrees of immersion tube inclination, amounting to a few mm of foil and pinhole displacement.

To assess the reliability of the three above proxy methods ($P_{\langle\varepsilon\rangle\mathrm{HBCm}}$, $P_{\langle\varepsilon\rangle\mathrm{TOT}}$, and $P_{\mathrm{ws}}$) in the presence of LoS misalignments, we employ them on a new dataset of 100 000 phantoms. This is generated using a new random seed with toroidally asymmetric mock-ups and with misaligned camera geometries included in the forward-calculated measurements.

The LoS misalignment is simulated by rotating the coordinates of the bolometer foils around the pinhole center point while the pinhole position is kept fixed (rigid displacements are neglected). Each one of the three cameras in the core bolometry system (figure 1) is rotated in this way around one of the three camera axes. The rotation angle is between $-2°$ and $+2°$, which roughly corresponds to a 5 mm maximum displacement of each foil with respect to the pinhole. Based on the rotated camera geometry, an alternative geometry matrix $G$ is computed via ray tracing. The misaligned geometry matrix is then applied as before to forward calculate the line-integrated power incident on the foil (equation (10)). The new proxy errors are plotted in figure 12(*a*) (third entry of figure 17), and noted in figure 12(*b*).

With misalignments, both the average $\delta_{\mathrm{ws}}$ error and its standard deviation are slightly increased compared to the same case without misalignments. Still, $P_{\mathrm{ws}}$ remains the better proxy overall.

In a similar manner, we can now quantify the impact of magnetic field errors on the $P_{\mathrm{rad}}$ proxy. Deviations from the assumed magnetic geometry can arise, for example, from error fields, iota corrections due to a finite toroidal plasma current, or a finite plasma $\beta$.

For this test, we assume that the field errors do not introduce any additional toroidal asymmetry. We define a new set of archetypes based on a different magnetic field geometry: the low-iota magnetic field configuration. The new low-iota archetypes are used to produce a dataset of 100 000 new low-iota mock-up phantoms, using the same set of nine toroidal profile modifiers. From these low-iota phantoms we forward calculate the line integrals $p$ as before. We apply the standard configuration $w_{\langle\varepsilon\rangle}$ and $w_{\mathrm{ws}}$ to estimate the $P_{\mathrm{rad}}$, hence simulating the conditions of a wrong magnetic field assumption. It should also be mentioned that the variation between the standard and the low-iota configuration is quite drastic for the purpose of this validation. This difference is surely more pronounced than

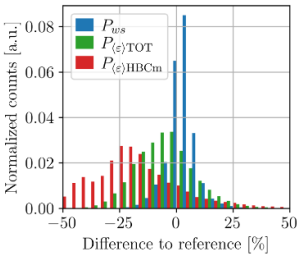


(a) Histogram of error $\delta$

| Tor. asym. mock-ups + $\vec{B}$ error | |
|---|---|
| $\delta_{\langle\varepsilon\rangle\mathrm{HBCm}}$ | $-15.8 \pm 19.9\,\%$ |
| $\delta_{\langle\varepsilon\rangle\mathrm{TOT}}$ | $-4.9 \pm 12.9\,\%$ |
| $\delta_{ws}$ | $+0.9 \pm 6.2\,\%$ |

(b) Averaged error $\delta$

**Figure 13.** Relative percentage error results for the validation case: toroidally asymmetric mock-ups with magnetic field errors.

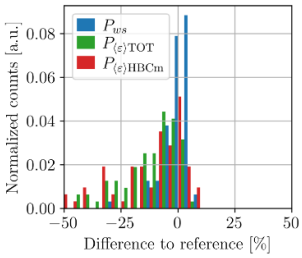


(a) Histogram of error $\delta$

| EMC3-EIRENE | |
|---|---|
| $\delta_{\langle\varepsilon\rangle\mathrm{HBCm}}$ | $-10.7 \pm 15.2\,\%$ |
| $\delta_{\langle\varepsilon\rangle\mathrm{TOT}}$ | $-11.8 \pm 12.0\,\%$ |
| $\delta_{ws}$ | $-2.8 \pm 5.8\,\%$ |

(b) Averaged error $\delta$

**Figure 14.** Relative percentage error results for the validation case: EMC3-EIRENE simulations of carbon impurity radiation.

the typical deviations from the set geometry in W7-X [28, 29]. The results of this test are reported in figure 13(fourth entry of figure 17).

The application of the standard configuration weights to the low-iota configuration dataset produces a similar outcome to the misalignment case. The performance of the weighted sum proxy $P_{\mathrm{ws}}$ shows again a small deterioration, but is maintained as the best proxy. Using a set of weights computed for the low-iota case yields performances similar to what was observed in the original mock-up situation (figure 10). This justifies the use of configuration-specific weights $w_{\langle\varepsilon\rangle}$ and $w_{\mathrm{ws}}$.

### 4.3. EMC3-EIRENE distributions

A final test is performed on a collection of 76 phantoms of carbon impurity radiation simulated with the EMC3-EIRENE code in the W7-X standard magnetic field configuration. The run settings cover a wide range of parameters:

- Heating power $P_{\mathrm{heat}} = 1 - 6\,\mathrm{MW}$
- Separatrix electron density $n_{\mathrm{sep}} = 1\text{–}4 \times 10^{19}\,\mathrm{m}^{-3}$
- Particle diffusion coefficient $D = 0.2\text{–}1.0\,\mathrm{m}^2\mathrm{s}^{-1}$
- Heat diffusion coefficient rescaled to satisfy $\chi = 3D$
- Radiated power fraction $f_{\mathrm{rad}} = 0.1\text{–}0.9$

In this case, the plasma emission presents many novel features compared to the training dataset. Here the toroidal evolution of the 2D poloidal radiation pattern is not a simple rescaling of the poloidal emission magnitude with the toroidal angle. The localized island emission sources (e.g. 'Emc3Mock' from 1 to 4 in figure 19 in the appendix) are individually enhanced or diminished at different toroidal angles [5, 30]. Additionally, the toroidal distributions in this set show more variability than the training profiles and less smooth gradients. This makes for characteristics that are considerably different from the condition the weights $w_{\mathrm{ws}}$ were optimized for. The results are shown in figure 14(fifth entry of figure 17).

We find that weighted sum is again providing the best total radiated power inference, both in terms of accuracy and precision. This further demonstrates the robustness of the weighted sum approach in different radiation conditions. When the simulation results are sufficiently trustworthy, the EMC3-EIRENE dataset itself can be used to calculate the optimal weights (including several radiating species and artificially added core emission) [12]. In comparison, the two average emissivity methods tend to underestimate the $P_{\mathrm{rad}}$ due to the highly localized island emission sources predicted by EMC3-EIRENE.

As anticipated in section 3.2, the $P_{\mathrm{ws}}$ robustness is dictated by the regularization parameter. At low regularization, the $P_{\mathrm{ws}}$ is highly optimized for the training features. On the other hand, its performance significantly worsens when the data differs from those of the training dataset. For example, a set of non-regularized ($\lambda = 0$) optimized weights would yield a slightly better $\delta_{\mathrm{ws}} = (-0.01 \pm 1.82)\%$ on the first validation case (asymmetric mock-ups). However, it would also yield a much larger spread on this fifth case (EMC3-EIRENE), with $\delta_{\mathrm{ws}} = (-0.8 \pm 13.4)\%$. The non-regularized performance would be degraded even more in the third and fourth validation case (with LoS misalignments and field errors), with a $\delta_{\mathrm{ws}}$ in the order of $\pm 20\%$. This justifies the introduction of a regularization parameter.

To summarize, the optimized weighted sum estimate exhibited the best accuracy and precision (respectively mean and standard deviation of the deviation $\delta$) across all the synthetic validation tests, as reported in figure 17. In the considered cases, the discrepancy between $P_{\mathrm{ws}}$ and the reference $P_{\mathrm{rad}}$ is typically small ($<5\%$) compared to the two alternative average emissivity method: all-channel $P_{\langle\varepsilon\rangle\mathrm{TOT}}$ (12%) and HBCm-only $P_{\langle\varepsilon\rangle\mathrm{HBCm}}$ ($>15\%$). If the radiation features presented by the phantoms (mock-ups and EMC3-EIRENE) are realistic, this robust performance should translate into a reliable proxy for $P_{\mathrm{rad}}$ in the experiment.

## 5. Experimental data

We now apply the proxy LoS weights to experimental bolometer line-integrated data from W7-X plasma discharges. The experimental dataset is introduced in section 5.1. In section 5.2, the results from the three different proxies are compared: the average emissivity estimate from the 32 HBCm channels $P_{\langle\varepsilon\rangle\mathrm{HBCm}}$, the all-channel average emissivity $P_{\langle\varepsilon\rangle\mathrm{TOT}}$, and the optimized weighted sum $P_{\mathrm{ws}}$. The scope of this comparison is to investigate the validity of each method as well as the real radiation distribution at W7-X.

### 5.1. Multiparametric dataset

All the data is collected from the last experimental campaign, January to March 2023. During this time, the divertor bolometry system capability was reduced due to hardware complications. Additionally, the CBCs have only been installed after the experimental campaign and therefore have not produced any experimental data yet. This leaves the core bolometry system, with 71 available resistive bolometer channels. The 71 respective average emissivity ($w_{\langle\varepsilon\rangle\mathrm{TOT}}$) and optimized ($w_{\mathrm{ws}}$) LoS weights are again calculated as explained in sections 2.1 and 2.2 respectively. Since all the 32 HBCm channels are utilized, the $P_{\langle\varepsilon\rangle\mathrm{HBCm}}$ performance is expected to be in line with the validation results.

Since the dataset is now experimental, the total radiated power is to be determined and there is no reference for our comparison. In addition, the divertor thermography data from this campaign was plagued by large noise levels and interferences from plasma radiation. So far, this prohibits any conclusive power balance test. To obtain a reference, we can perform 2D tomographic inversions of the radiation distribution in the FoV of the core bolometry system to retrieve the tomographic proxy $P_{\mathrm{tomo}}$. As explained in section 2.3, this represents our best estimate of the plasma radiated power in the triangular symmetry plane. Thus, we can consider $P_{\mathrm{tomo}}$ our reference to which the three alternative proxies must compare.

We select 150 separate plasma discharges performed in standard magnetic field configuration (forward field direction). All are purely ECR-heated and contain both intrinsic carbon and seeded impurity radiation, either through gas (N, Ne, Ar) [31], LBO [32], or pellet (TESPEL) [33] injection. These discharges cover a wide range of plasma scenarios including plasma startup and termination, density and gas seeding ramps into detachment, applied power steps, and small plasmas. Both long (>20 s) and short (<5 s) pulse durations are included. The experimental line-integrated power measurements are averaged in time with 100 ms intervals (see for example figure 3(*c*)). On the same time intervals, all the relevant experimental plasma parameters are time-averaged and collected. At each data point, tomographic inversion on the line-integrated power data from the core bolometry system (figure 3(*b*)). The inversion problem is solved with the use of the RGS-GPT method [18]. Lastly, the alternative experimental proxies $P_{\langle\varepsilon\rangle\mathrm{HBCm}}$, $P_{\langle\varepsilon\rangle\mathrm{TOT}}$, and $P_{\mathrm{ws}}$ are also calculated from the line-integrated bolometer data. If the plasma diamagnetic energy $W_{\mathrm{dia}}$ varies by more than 1% across the 100 ms time interval or if $\frac{P_{\mathrm{tomo}}}{P_{\mathrm{heat}}} > 1$, the plasma conditions are considered non-stationary and the corresponding data point is excluded. The final result is a multiparametric dataset of ∼13 000 accepted entries.

### 5.2. Comparison to tomographic $P_{\mathrm{rad}}$ proxy

The aim now is to assess whether the poloidal features of the training dataset are similar to the experiment, and how reliably the optimized weights can recover the average poloidal plasma emissivity. Here the reference is $P_{\mathrm{tomo}}$, which is assumed to be an exact reflection of the poloidal radiation distribution (no inversion error).

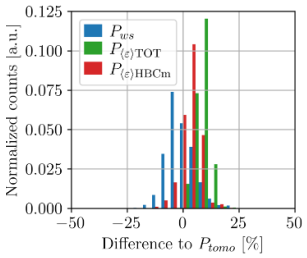


(a) Histogram of error $\delta$

| Experimental (core bol. sys.) | |
|---|---|
| $\delta_{\langle\varepsilon\rangle\mathrm{HBCm}}$ | $+5.4 \pm 4.6\,\%$ |
| $\delta_{\langle\varepsilon\rangle\mathrm{TOT}}$ | $+8.9 \pm 3.5\,\%$ |
| $\delta_{ws}$ | $-3.2 \pm 6.3\,\%$ |

(b) Averaged error $\delta$

**Figure 15.** Relative percentage error results for the validation case: experimental data from the core bolometry system (triangular plane).

The results of this comparison are reported in figure 15(last entry of figure 17. Although the 71 weights $w_{\mathrm{ws}}$ are optimized for the synthetic dataset detailed in section 3, its deviation from $P_{\mathrm{tomo}}$ is of only a few percentages. This indicates that the phantoms used in the validation section are sufficiently representative of the real poloidal radiation features in the experiment.

Regarding the average emissivity proxies, we notice how the deviation to the reference $P_{\mathrm{tomo}}$ are now on an overall smaller scale ($\pm 10\%$) compared to the validation tests of Sec 4 ($\pm 25\%$). One reason could be that the error on the reference is so far assumed to be zero. If a finite uncertainty on $P_{\mathrm{tomo}}$ was introduced, the error distribution of the alternative $P_{\mathrm{rad}}$ estimates would be amplified.

The core-only $P_{\langle\varepsilon\rangle\mathrm{HBCm}}$ overestimates $P_{\mathrm{tomo}}$ by 5% on average. In comparison, the average overestimation is increased to 9% when applying $P_{\langle\varepsilon\rangle\mathrm{TOT}}$. Past studies have demonstrated the tendency of the vertical camera VBC (see figure 1) to overestimate the total $P_{\mathrm{rad}}$ when the up-down asymmetry of the plasma emission is dominant on the lower side [24]. This is often the case in the W7-X forward field standard configuration [8], which is the only configuration considered here.

During this test on experimental data, the same $P_{\mathrm{ws}}$ regularization factor of $\lambda = 10^{-4}$ was maintained from the synthetic validation cases. Taking advantage of the flexibility of the optimization procedure, we can now adjust the sensitivity of the method to match the new experimental radiation features. We repeat the test of figure 15 multiple times, scanning over a range of $\lambda$ values. We track the performance resulting from each set of optimized weights to single out the $\lambda$ value for which the relative percentage error to $P_{\mathrm{tomo}}$ is minimized. A significantly reduced relative percentage error $\delta_{\mathrm{ws}}$ is achieved when the regularization factor is raised to $\lambda = 2.3 \times 10^{-4}$. Figure 16 reports a comparison between this re-calibrated optimized weighted sum $P_{\mathrm{ws\,(recal)}}$ (pink) and the lower regularization case (blue) from figure 15.

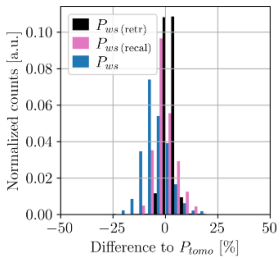


(a) Histogram of error $\delta$

| Experimental (core bol. sys.) | |
|---|---|
| $\delta_{ws}$ | $-3.2 \pm 6.3\,\%$ |
| $\delta_{ws\,(\mathrm{recal})}$ | $+0.06 \pm 5.14\,\%$ |
| $\delta_{ws\,(\mathrm{retr})}$ | $-0.05 \pm 2.71\,\%$ |

(b) Averaged error $\delta$

**Figure 16.** Relative percentage error results for the validation case: experimental data from the core bolometry system (triangular plane). In this case, the optimized weighted sum is re-calibrated by adjusting its regularization factor (pink) or re-trained (black) to match the $P_{\mathrm{tomo}}$ data.

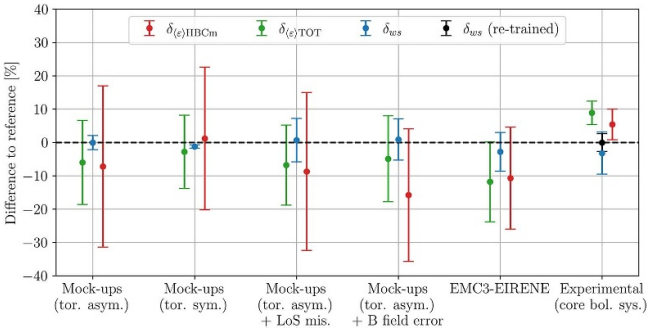


**Figure 17.** Overview on the average relative percentage error $\delta$ and its standard deviation from the three total radiated power proxies: HBCm-only average emissivity (red), all-channel average emissivity (green), and weighted sum (blue). Each entry in the horizontal axis is a different test case. On the far right-hand side, the analysis is limited to experimental data from the core bolometry system, and the reference is $P_{\mathrm{tomo}}$. Only the standard magnetic field configuration is considered.

Finally, the optimal LoS weights can be trained on the experimental data directly. In this case, the target ($b$ in equation (7)) are the 13 000 $P_{\mathrm{tomo}}$ values from the multiparametric dataset. The input data ($A$ in equation (7)) are the corresponding line integrals. We call this re-trained optimized weighted sum $P_{\mathrm{ws\,(retr)}}$, shown again in figure 16 and figure 17(black). Its performance surpasses the one of $P_{\mathrm{ws\,(recal)}}$, achieving 3% relative percentage error. The implication is that the re-trained $P_{\mathrm{ws}}$ estimate could be used in the experiment to retrieve the triangular plane $P_{\mathrm{tomo}}$ without the need to formulate prior assumptions or perform tomography. $P_{\mathrm{ws}}$ is computed from a simple and fast weighted summation, which would make this proxy readily available post-discharge or even in real-time (order of $\mu$s run time).

## 6. Conclusions

A set of optimized LoS weights was applied to quantify the total radiated power of several synthetic datasets in a validation study. The datasets consisted of mock-up radiated power patterns as well as EMC3-EIRENE computed carbon impurity radiation, and included poloidal and toroidal radiation asymmetries, random noise, camera misalignments, and changes in the magnetic field geometry. In all studied cases, the optimized weights exhibited the best performance ($<5\%$ average uncertainty) when compared to the current average emissivity method ($>15\%$). Lastly, the optimized weights were applied to experimental data and compared to extrapolations from tomography. When limited to the triangular plane, a set of weights optimized based on the experimental line integrals was capable of providing a real-time capable alternative to the tomographic $P_{\mathrm{rad}}$ (order of $\mu$s run time, $< 5\%$ error). In the next campaign, future studies using more bolometer sightlines and including power balance will provide a more complete and conclusive validation for this approach.

## Data availability statement

The data that support the findings of this study are available from the corresponding author upon reasonable request.

## Acknowledgment

This work has been carried out within the framework of the EUROfusion Consortium, funded by the European Union via the Euratom Research and Training Programme (Grant Agreement No 101052200—EUROfusion). Views and opinions expressed are however those of the author(s) only and do not necessarily reflect those of the European Union or the European Commission. Neither the European Union nor the European Commission can be held responsible for them. This research was supported by the NINS-DAAD International Personal Exchange Program, MEXT Grant in Aide # KA22KK0039 and NIFS Grant in Aide # SIU004. The authors thank V. Winters, D. Bold, N. Maaziz, and V. Perseo for their feedback regarding plasma modeling and analysis of experimental plasma discharges.

## Appendix. Sources of error for $P_{\langle\varepsilon\rangle\mathrm{HBCm}}$

Understanding the main sources of error for the current—HBCm-only average emissivity—estimate can aid in designing an improved method and estimating the proxy error bars. Figure 11($b$) (red) shows the results when the estimate is applied to a set of 100 000 toroidally uniform mock-up phantoms. Here we focus on the $P_{\langle\varepsilon\rangle\mathrm{HBCm}}$ case, a closeup of which is reported in figure 18($b$). The average error and standard deviation are listed in figure 11($b$).

We find that the error distribution of the proxy $\delta_{\langle\varepsilon\rangle\mathrm{HBCm}}$ peaks between $-20\%$ and $-10\%$. More seldom, the method can severely overestimate the total radiated power for $\delta_{\langle\varepsilon\rangle\mathrm{HBCm}} > 40\%$. Since the toroidal variation of the radiated

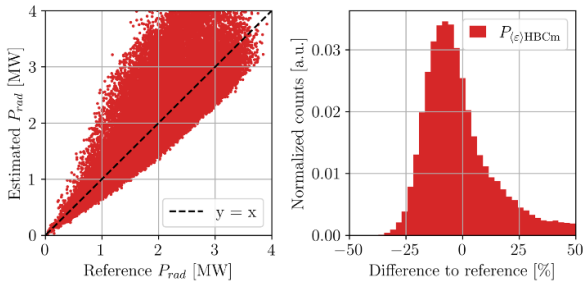


(a) Comparison of $P_{rad}$ methods (b) Histogram of error $\delta$

**Figure 18.** (Left) $P_{\langle\varepsilon\rangle\mathrm{HBCm}}$ estimate of the total radiated power plotted against the corresponding $P_{\mathrm{rad}}$ reference values. The emissivity distribution is assumed to be toroidally symmetric. A dashed line indicates the exact $y = x$ solution. (Right) Histogram of the percentage errors to the relative reference $\delta_{\langle\varepsilon\rangle\mathrm{HBCm}}$.

power density is negligible, the observed error distribution is purely due to the poloidal emissivity pattern.

Every phantom employed in the test is generated from a random combination of two edge and two core archetypal radiation patterns, following the logic explained in section 3.1. We now turn our attention towards the average error contribution of each archetype to $\delta_{\langle\varepsilon\rangle\mathrm{HBCm}}$. We track the four archetypes constituting each one of the 100 000 phantoms and their associated error $\delta_{\langle\varepsilon\rangle\mathrm{HBCm}}$. Since the archetypes are picked randomly, each archetype appears with roughly the same frequency in the pool of phantoms. The archetype occurrences are then counted in a weighted histogram, with the weight being the resulting $\delta_{\langle\varepsilon\rangle\mathrm{HBCm}}$.

There is a large degree of variation in the error contribution carried by each archetype to the HBCm-proxy, as shown in figure 21. The largest inaccuracy by far is associated with phantoms containing a strong emission component at the outboard $X$-point (e.g. 'Xp1' and 'InRing' in figure 19). The average emissivity of phantoms containing these features is strongly overestimated, causing the positive-error tail of figure 10(*a*). Simply removing these two archetypes from the pool causes the overestimation tail to almost completely vanish. Underestimation is statistically more common and less severe. The archetypes associated with underestimation are inboard side-dominant (e.g. 'Xp3', 'Xp4', and 'OutRing' in figure 19). This is consistent with previous results from a smaller case study [24]. As expected, there seems to be no dependence on the upper vs. lower poloidal asymmetry.

Applying a toroidal profile modifier introduces a further systematic error in the $P_{\mathrm{rad}}$ estimation, depending on the kind of asymmetry. For asymmetries peaking in the divertor (core) region, the scatter points move downwards (upwards) relative to the $y = x$ line. This systematic underestimation (overestimation) of the $P_{\mathrm{rad}}$ corresponds to a rigid shift of the $\delta$ histogram towards the left (right). When a multitude of different toroidal asymmetries are present, the overall effect is a larger spread of the $P_{\mathrm{rad}}$ proxy. The difference is noticeable when comparing figure 10 with figure 11(red histogram).

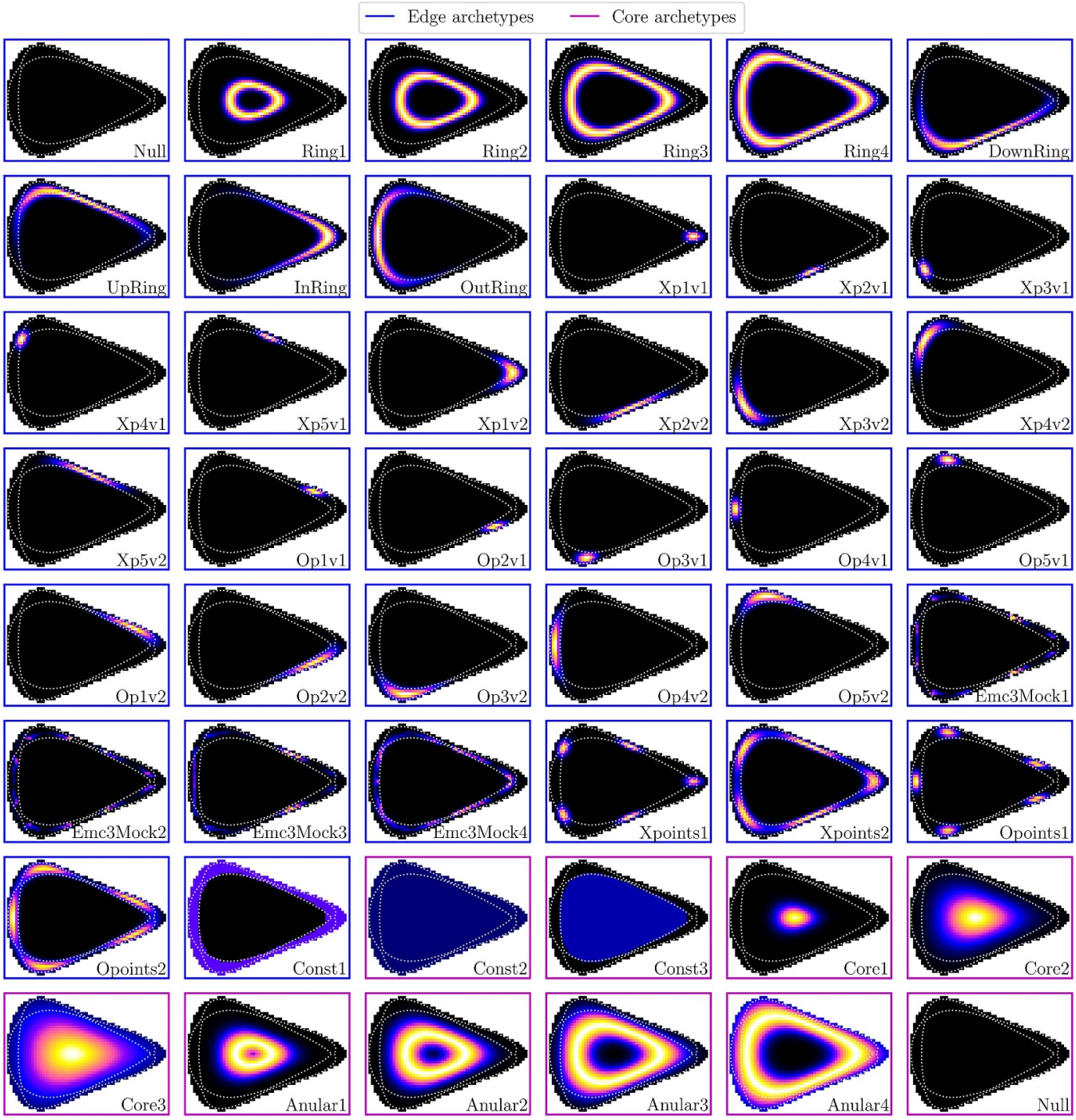


**Figure 19.** Archetypal emissivity distributions used for generating the synthetic dataset of mock-ups. The color bar of each radiation pattern is re-normalized to highlight the qualitative radiation distribution. Edge emission patterns (first seven rows) are indicated in blue while core ones (last three rows) are indicated in pink. The archetypes contain basic radiation features identified from experiments and EMC3-EIRENE simulated impurity radiation.

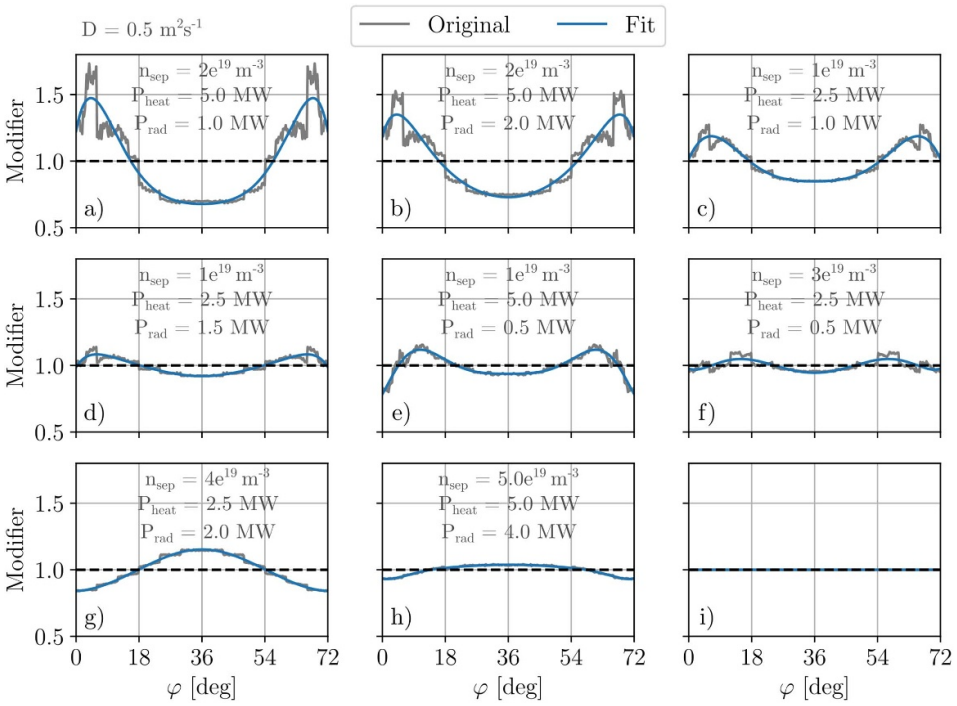


**Figure 20.** Toroidal profile modifier employed to control the toroidal distribution of the emissivity phantoms. Each modifier from (*a*) to (*h*) is defined based on the poloidally-averaged plasma emissivity (grey line) computed from a different EMC3-EIRENE simulation of carbon impurity radiation. The toroidal profile is fitted with a polynomial function of the toroidal angle $\varphi$ (blue line) and the average is normalized to 1. The run settings are noted on each panel. Profile (*i*) is a mock-up representing ideal toroidal symmetry.

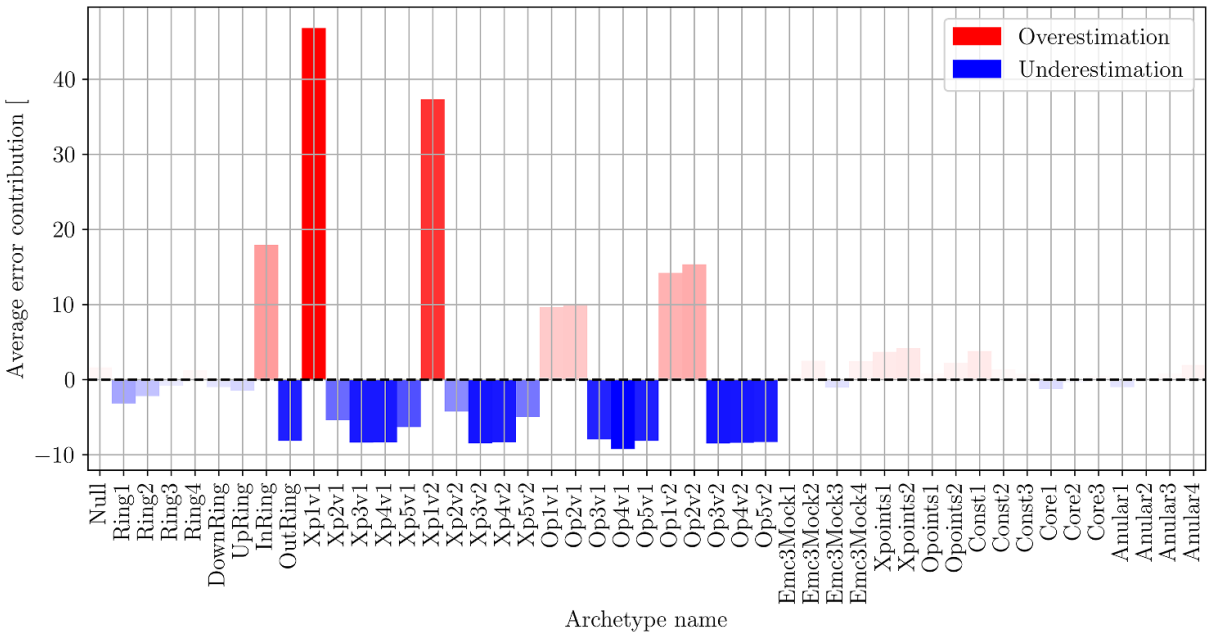


**Figure 21.** Average contribution of each archetype to the error in the current total radiated power proxy. The proxy is calculated from the average emissivity method on HBCm ($P_{\langle\varepsilon\rangle\mathrm{HBCm}}$). Each nametag in the *x* axis refers to one radiation archetype reported in figure 19. The error ($\delta_{\langle\varepsilon\rangle\mathrm{HBCm}}$) is expressed as a percentage relative to the reference $P_{\mathrm{rad}}$ value. Overestimation (underestimation) of this value is generally associated with outboard (inboard) dominant components.

## ORCID iDs

G. Partesotti https://orcid.org/0009-0008-9465-7885
F. Reimold https://orcid.org/0000-0003-4251-7924
A. Tsikouras https://orcid.org/0009-0008-9677-3302
D. Zhang https://orcid.org/0000-0002-5800-4907
G. Kawamura https://orcid.org/0000-0002-9117-5898
B.J. Peterson https://orcid.org/0009-0002-8230-0121

## References

[1] Wischmeier M. 2015 *J. Nucl. Mater.* **463** 22
[2] Schmitz O. *et al* 2020 *Nucl. Fusion* **61** 016026
[3] Giannone L., Queen D., Hellman F. and Fuchs J. 2005 *Plasma Phys. Control. Fusion* **47** 2123
[4] Kallenbach A., Bernert M., Eich T., Fuchs J., Giannone L., Herrmann A., Schweinzer J. and Treutterer W. (the ASDEX Upgrade Team) 2012 *Nucl. Fusion* **52** 122003
[5] Partesotti G., Reimold F., Ruhnau J., Tsikouras A., Kubeneck D., Zhang D. and Geißler P. (W7-X Team) 2024 *Rev. Sci. Instrum.* **95** 103503
[6] Zhang D. *et al* 2010 *Rev. Sci. Instrum.* **81** 10E134
[7] Ferreira D.R., Carvalho P.J., Carvalho I.S., Stuart C. and Lomas P.J. (JET Contributors) 2021 *Fusion Eng. Des.* **164** 112179
[8] Zhang D. *et al* 2021 *Nucl. Fusion* **61** 116043
[9] Devynck P. *et al* 2021 *J. Phys. Commun.* **5** 095008
[10] Ingesson L., Rapp J. and Matthews G. 2003 *J. Nucl. Mater.* **313-316** 1173
[11] Kobayashi M. *et al* 2013 *Nucl. Fusion* **53** 093032
[12] van de Giessen P.L., Kawamura G., Borling S., Mukai K. and Peterson B.J. 2021 *Rev. Sci. Instrum.* **92** 033518
[13] Peterson B.J. *et al* 2021 *Nucl. Mater. Energy* **26** 100848
[14] Sano R., Peterson B.J., Teranishi M., Iwama N., Kobayashi M., Mukai K. and Pandya S.N. 2016 *Rev. Sci. Instrum.* **87** 053502
[15] Mukai K., Kawamura G., Masuzaki S., Hayashi Y., Tanaka H., Peterson B., Oishi T., Suzuki C., Kobayashi M. and Munechika K. 2022 *Nucl. Mater. Energy* **33** 101294
[16] Feng Y. *et al* 2014 *Contribut. Plasma Phys.* **54** 426–31
[17] Partesotti G., Reimold F., Wurden G.A., Mukai K., Peterson B.J., Winters V., Zhang D. and Demby A. 2023 Investigation of radiation distribution inW7-X with an infrared video bolometer camera note poster contribution at FuseNet PhD Event
[18] Partesotti G., Reimold F., Wurden G.A., Peterson B.J., Zhang D. and Mukai K. 2024 Assessing the toroidal radiation distribution at Wendelstein 7-X by combining Gaussian Process Tomography and field line mapping *Nucl. Mater. Energy.* accepted
[19] Zhang D., Burhenn R., Feng Y., Koenig R., Buttenschön B., Beidler C., Hacker P., Reimold F., Thomsen H., Laube R. 2021 *Nucl. Fusion* **61** 126002
[20] Kriete D., Pandey A., Perseo V., Schmitt J., Ennis D., Gradic D., Hammond K., Jakubowski M., Killer C. and König R. 2023 *Nucl. Fusion* **63** 026022
[21] Zhang D. *et al* 2023 *Plasma Phys. Control. Fusion* **65** 105006
[22] Loffelmann V., Mlynar J., Imrisek M., Mazon D., Jardin A., Weinzettl V. and Hron M. 2016 *Fusion Sci. Technol.* **69** 505
[23] David P., Bernert M., Pütterich T., Fuchs C., Glöggler S. and Eich T. (the ASDEX Upgrade Team) 2021 *Nucl. Fusion* **61** 066025
[24] Maaziz N. and Reimold F. 2021 Improving power balance on Wendelstein 7-X *Technical Report* IPP 2024-10 (Max-Planck Institute for Plasma Physics)
[25] Grahl M., Svensson J., Werner A., Andreeva T., Bozhenkov S., Drevlak M., Geiger J., Krychowiak M. and Turkin Y. 2018 *IEEE Trans. Plasma Sci.* **46** 1114—9
[26] Asakura N., Hoshino K., Kakudate S., Subba F., Vorpahl C., Homma Y., Utoh H., Someya Y., Sakamoto Y. and Hiwatari R. 2021 *Nucl. Fusion* **61** 126057
[27] Xiang L., Militello F., Moulton D., Subba F., Aho-Mantila L., Coster D., Wensing M., Lunt T., Wischmeier M. and Reimerdes H. 2021 *Nucl. Fusion* **61** 076007
[28] Lazerson S.A., Bozhenkov S., Israeli B., Otte M., Niemann H., Bykov V., Endler M., Andreeva T., Ali A. and Drewelow P. 2018 *Plasma Phys. Control. Fusion* **60** 124002
[29] Killer C., Gao Y., Perseo V., Rudischhauser L., Hammond K., Buttenschön B., Barbui T., Blackwell B.D., Brunner K.-J. and Drews P. 2019 *Plasma Phys. Control. Fusion* **61** 125014
[30] Geißler P. 2022 Investigating radiation and its distribution in W7X with EMC3/EIRENE *Technical Report* IPP 2024-26 (Max-Planck Institute for Plasma Physics)
[31] Krychowiak M., König R., Barbui T., Brezinsek S., Brunner J., Effenberg F., Endler M., Feng Y., Flom E. and Gao Y. 2023 *Nucl. Mater. Energy* **34** 101363
[32] Wegner T., Geiger B., Kunkel F., Burhenn R., Schröder T., Biedermann C., Buttenschön B., Cseh G., Drews P. and Grulke O. 2018 *Rev. Sci. Instrum.* **89** 073505
[33] Laube R., Bussiahn R., Tamura N. and McCarthy K.J. 2020 *Fusion Eng. Des.* **150** 111259